NANO LETTERS

Communication

Integrated high-performance infrared phototransistor arrays composed of nonlayered PbS-MoS2 heterostructures with edge contacts

yao wen, Lei Yin, Peng He, Zhenxing Wang, XianKun Zhang, Qisheng Wang, Tofik Ahmed Shifa, Kai Xu, Fengmei Wang, Xueying Zhan, Feng Wang, Chao Jiang, and Jun He

Nano Lett., **Just Accepted Manuscript** • DOI: 10.1021/acs.nanolett.6b02881 • Publication Date (Web): 29 Sep 2016

Just Accepted

ACS Publications

Nano Letters is published by the American Chemical Society. 1155 Sixteenth Street N.W., Washington, DC 20036

Integrated high-performance infrared phototransistor arrays composed of nonlayered PbS-MoS_2 heterostructures with edge contacts

Yao Wen,[1,2,4]† Lei Yin,[1,3,4]† Peng He,[5] Zhenxing Wang,[1,3] XianKun Zhang,[6] Qisheng Wang,[7] Tofik Ahmed Shifa,[1,3,4] Kai Xu,[1,3,4] Fengmei Wang,[1,3,4] Xueying Zhan,[1,3] Feng Wang,[1,3,4] Chao Jiang[1,2] and Jun He[1,3]*

[1]CAS Center for Excellence in Nanoscience, [2]CAS Key Laboratory for Standardization and Measurement for Nanotechnology, [3]CAS Key Laboratory of Nanosystem and Hierarchical Fabrication, National Center for Nanoscience and Technology, Beijing 100190, China

[4]University of Chinese Academy of Sciences, Beijing 100049, China

[5]State Key Laboratory of Chemical Resource Engineering, Beijing University of Chemical Technology, Beijing 100029, China

[6]State Key Laboratory for Advanced Metals and Materials, School of Materials Science and Engineering, University of Science and Technology Beijing, Beijing 100083, China

[7]Department of Electrical and Computer Engineering, National University of Singapore, 117576 Singapore

Table of Contents Graphic

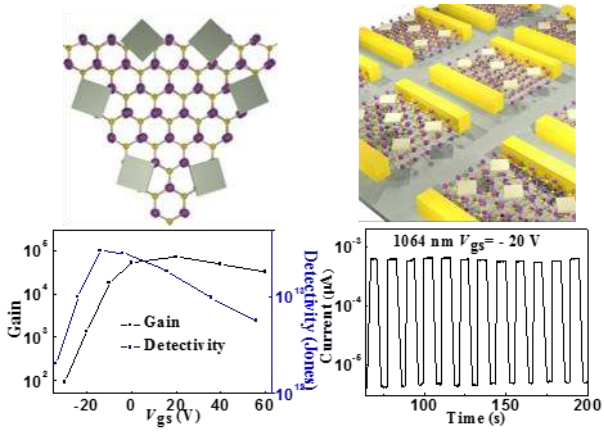

ABSTRACT**:** Molybdenum disulfide (MoS_2) has attracted a great deal of attention in optoelectronic applications due to its high mobility, low off-state current and high on/off ratio. However, its intrinsic large bandgap limits its application in infrared detection. Here, we have developed a high-performance infrared photodetector by integrating non-layered PbS and layered MoS_2 nanostructures via van der Waals epitaxy. Density functional theory (DFT) calculations indicate that PbS nanoplates are in contact with MoS_2 edges through strong chemical hybridization, which is expected to offer a fast transmission path for carriers that

enhances the response speed. The phototransistor exhibits a fast response (τ_{rising}= τ_{decay}= 7.8 ms) as well as high photoresponsivity (4.5×10^4 AW^{-1}) and I_{light}/I_{dark} (1.3×10^2) in the near-infrared spectral region at room temperature. In particular, the detectivity (D*) is as high as 3×10^{13} Jones, which is even better than that of commercial Si and InGaAs photodetectors. Furthermore, by controlling the growth and micro-fabrication patterning, periodic device arrays of PbS-MoS_2 that are capable of infrared detection are achieved on Si/SiO_2 substrates. Our work provides a possible method for the integration of photodetector arrays on Si-based electronic devices and lays a solid foundation for the practical applications of MoS_2-based devices in the future.

KEYWORDS: non-layered PbS-MoS_2 heterostructure, edge contact, integration, infrared phototransistor

Molybdenum disulfide (MoS_2) has shown remarkable potential in optoelectronic devices due to its high mobility,[1, 2] low off-state current and high on/off ratio.[3-14] Despite such superb performance, its intrinsically large bandgap limits its application in infrared detection. Recently, a hybrid MoS_2–PbS colloidal quantum dot (QD) phototransistor achieved an ultrahigh photoresponsivity of 10^3 AW^{-1} at 1500 nm.[15] PbS exhibits a broad spectral response from the UV to mid-IR region, which is highly desired for various applications, including thermal imaging, telecommunications, biological imaging, remote sensing and environmental monitoring.[16, 17] Due to its excellent infrared photoconductive properties, the photoelectrical response of MoS_2 extends to the infrared spectral region. However, hybrid phototransistors have some disadvantages: (1) they suffer from large dark currents owing to the surface n-type doping from 1,2-ethanedithiol (EDT), which lowers the ratio of the light to dark current (I_{light}/I_{dark}) and limits detectivity. (2) They have a modest response speed (τ_{decay}= 0.3-0.4 s) due to the presence of crystal boundaries between QDs and the relatively long van der Waals interaction distance in the interface.[15, 18] In addition, the vdW gap in the interface increases the tunnel barrier of carriers from PbS to MoS_2.[19] More recently, a few-layer MoS_2 phototransistor driven by ferroelectrics exhibited a fast response speed of up to 2 ms and high detectivity of 10^{12} Jones at 635 nm.[20] However, it exhibited a very poor responsivity (< 1 AW^{-1} at 1500 nm) due to the weak light harvesting ability of the indirect bandgap MoS_2 in the infrared region.[21] Despite the tremendous progress in the synthesis and application of MoS_2 for infrared detection, there remains a huge challenge of simultaneously achieving fast response speed, high photoresponsivity and detectivity in the infrared spectral region. Furthermore, detector technologies should be

compatible with traditional complementary metal-oxide semiconductor (CMOS) electronics for integration into high-sensitivity sensing and imaging systems.[18, 22] Periodic arrays have shown superior performance in active matrix displays and sensor arrays, which require minimal cross-talk between neighboring devices.[23-29] Therefore, integrating the non-layered PbS-MoS_2 nanostructure and forming a controllable heterostructure on Si chips is a crucial subject for their practical applications.

Here, we demonstrate a heterostructure phototransistor composed of non-layered PbS nanoplates that are edge-contacted with a layered MoS_2 sheet. The PbS nanoplates are in contact with the edges of MoS_2 along the <110> direction. Combined with density functional theory (DFT) calculations, we elucidate that PbS nanoplates are in contact with MoS_2 edges via a strong chemical hybridization, which is expected to offer a fast transmission path for carriers to enhance the response speed. The device presents fast response (τ_{rising}= τ_{decay}=7.8 ms), high responsivity (4.5×10^4 A/W) and I_{light}/I_{dark} (1.3×10^2), and an ultrahigh detectivity of 3×10^{13} Jones in the infrared spectral region. Furthermore, by controlling the growth and micro-fabrication patterning, periodic device arrays of MoS_2-PbS that are capable of infrared detection are achieved on Si/SiO_2 substrates. Our work paves a new way for the fabrication of high-performance infrared photodetectors and also provides a possible method for the integration of photodetector arrays on Si-based electronic devices.

Figure 1a exhibits the schematic illustration of epitaxial growth of non-layered PbS nanoplates-MoS_2 heterostructures, which were prepared by low-pressure chemical vapor deposition (LPCVD). The PbS powder was thermally evaporated into vapor molecules and then self-assembled into single crystalline nanoplates on MoS_2. MoS_2 was synthesized by chemical vapor deposition (CVD) from molybdenum trioxide (MoO_3) and pure sulfur powders (more details are presented in the Supplementary information details). Interestingly, PbS nanoplates selectively grew along the edge of the MoS_2 triangle (as observed in the optical microscope images in Figure 1b). The thickness of MoS_2 is approximately 3 nm. The selected area electron diffraction (SAED) pattern exhibits a perfect hexagonal arrangement, which clearly reveals the high crystallinity of the CVD MoS_2, as shown in supplementary information Figure S1. The corresponding Raman spectra is presented in supplementary information Figure S2 with a distance of 23 cm^{-1} between two vibrating modes at 386 and 409 cm^{-1}, which are attributed to CVD MoS_2 E_{2g} and A_{1g} modes, respectively.[30] The sharp spectral features indicate the inexistence of substantial disorders in the CVD MoS_2. To verify that PbS nanoplates unambiguously have

edge-contact with MoS_2, scanning electron microscopy (SEM) and atomic force microscopy (AFM) were employed, and the images are depicted in the inset of Figure 1b, Figure 1c and Figure S3. Almost all PbS nanoplates contacted with the MoS_2 triangle edge along the diagonal of the square PbS nanoplates. The selective growth behavior could be explained by the fact that the triangular MoS_2 edge with an unsaturated dangling bond is favorable for initial nucleation. The mechanism behind this can be further explained via density functional theory (DFT) calculations, as shown in Figure 4. The high-resolution transmission electron microscopy (HRTEM) image (Figure 1d) demonstrates that the PbS nanoplate is well-defined single crystalline with clear crystal fringes of (200) planes. As shown in the inset of Figure 1d, the SAED pattern clearly reveals the cubic symmetry of the nanoplates. The standard square geometry confirms the intrinsic cubic crystal structure of PbS nanoplates. Therefore, PbS nanoplates have (002) top and bottom planes and contact with the MoS_2 triangle edges along their <110> direction. Van der Waals epitaxy involves a weak van der Waals interaction between two adjacent layers. Here, MoS_2 is used as the growth substrate because it is a layered material with a highly smooth and chemically passivated surface.[31-33] The standard square geometry of PbS nanoplates confirms the nature of van der Waals epitaxy as PbS shows a lattice mismatch with MoS_2; this is less likely in conventional epitaxial growth. In addition, as shown in Figure S4 (a-c), the time-dependent growth of PbS-MoS_2 heterostructures exhibits the following features: (1) PbS nuclei are observed at the MoS_2 edge (t=30 S), (2) Small PbS particles are formed and parts of the nanoplates tend to coalesce with each other (t=90 S), and (3) square-shaped PbS nanoplatelets are formed (t=180 S). On the basis of the gradual evolution in the morphology, we propose that PbS is formed through a mechanism based on van der Waals epitaxy. Specifically, this formation phenomenon is common for a van der Waals epitaxy-based mechanism.[29, 34, 35] Figure 1e and Figure 1f exhibit the statistics of the lateral dimension distribution and thickness distribution of the PbS nanoplates on MoS_2. The lateral dimension and thickness distribution of nanoplates range from 150 to 750 nm and 20 to 80 nm, respectively. Compared with previous van der Waals epitaxy methods, the PbS nanoplates become thicker under the same reaction parameters. This indicates that the edge contact with MoS_2 strongly affects the morphology of PbS nanoplates.

To systematically investigate the optoelectronic properties of PbS-MoS_2 heterostructures, back-gated phototransistors were fabricated on n-doped silicon substrates. Electron beam lithography (EBL) was

employed to pattern source/drain electrodes on as-synthesized PbS-MoS_2 heterostructures. Subsequently, metal electrodes (Cr/Au, 10 nm/ 60 nm) were deposited by thermal evaporation. The schematic of a typical device is shown in Figure 2a. The transfer characteristics (I_{ds}-V_{gs}) were measured under laser illumination (wavelength, λ = 800 nm) with various power densities at V_{ds} = 2 V, T = 300 K and the results are depicted in Figure 2b. The channel length and channel width are 3.2 and 1.3 µm, respectively. The electron mobility is estimated as 1.4 $cm^2\ V^{-1}\ s^{-1}$. For an excitation wavelength of 800 nm, photogenerated carriers mainly originate from PbS nanoplates, which represent the photosensitive component in the heterostructures is PbS nanoplates(bandgap, E_g = 0.4 eV)[36], rather than MoS_2 (E_g = 1.2 eV)[37]. We compare the optoelectronic performance between MoS_2 devices and PbS-MoS_2 heterostructures, as shown in Figure S5 (a-b). Although the power density is as high as 604 mW/cm^2, the multilayer MoS_2 device shows modest photoresponse due to the weak light harvesting ability of the indirect bandgap material, as depicted in Figure S5 a. Compared with MoS_2 devices, the PbS-MoS_2 heterostructure exhibits a superior photoresponse when P = 178 mW/cm^2. In Figure S5 b, it is observed that the rise and decay time of the photocurrent after switching exceeds 5 s for the MoS_2 device at P= 604 mW/cm^2, which is similar to their analogues.[21] In addition, a steady photoswitching behavior was observed upon excitation by a 1064 nm and 1340 nm laser with power densities of 124 and 145 mW/cm^2, respectively. However, MoS_2 is not involved in photocarrier generation due to its bandgap (1.2 eV = 1033 nm).[37] Therefore, photogenerated carriers mainly originate from PbS nanoplates in the heterostructures. Furthermore, the effective irradiated area includes both the exposed MoS_2 and PbS-MoS_2 heterostructure when responsivity (R) is obtained, as observed in Figure 2d. Therefore, photogenerated electrons are transferred from PbS to MoS_2, which results in a pronounced photoresponse, as observed in the inset of Figure 2b. The linear output characteristic (I_{ds}-V_{ds}) curves at different power densities are displayed in Figure 2c; they indicate ohmic-like contact behavior. Responsivity (R) is one of the most important parameters for photodetectors, and it is defined by the following formula: $R = I_{ph}/PS$, where I_{ph} is the photocurrent ($I_{ph} = I_{light} - I_{dark}$), P is the incident power density and S is the effective illuminated area. The effective irradiated area is approximately 2.98 μm^2. In Figure 2d, the responsivity of our device is plotted as a function of the applied back-gated voltage at different power densities. We observe that the responsivity does not monotonically increase as the gate voltage increases at a fixed laser power; the responsivity is as high as 4.5×10^4 A/W when V_{gs} = 20 V and P = 0.15

mW/cm^2. However, the responsivity decreases when V_{gs}> 20 V because of the reduced photocurrent, which is due to the high dark current at the on-state. The gate-modulated behavior of the responsivity indicate that the gate voltages effectively control the state of photodetectors, which highlights its potential in video frame rate imaging applications.[38] The specific detectivity (D^*) can be calculated by $D^* = RS^{1/2}/(2qI_d)^{1/2}$, where R, S, q and I_d are the responsivity, the effective illuminated area, the electron charge, and the dark current, respectively. Figure 2e shows that the responsivity and detectivity of this device increase linearly with the laser power, which indicates that photogenerated electron-hole pairs are effectively separated. A similar gate-tunable behavior is also observed for the photo-gain (G) and detectivity, as shown in Figure 2f. The maximum G of 7×10^4 is obtained at V_{gs} = 20 V and P = 0.15 mW/cm^2. However, we note that the peak value of the detectivity of 3×10^{13} Jones shifts to V_{gs} = 0 V because superior D^* is jointly determined by high responsivity and low dark current. These impressive results indicate an excellent performance of our photodetectors based on PbS-MoS_2 heterostructures in the near-infrared region, which is significantly superior to the performance of their analogues with hybrid structures and even better than the performance of commercial Si- and InGaAs-based devices. A comparison of critical performance indicators is provided in Table 1.

To study the photoswitching characteristic and the stability of the photodetectors based on PbS-MoS_2 heterostructures, the time-resolved photoresponse in the near-infrared region was measured. In Figure 3a, the current periodically changes with the alternate on-off switching of the laser, which indicates a highly stable and reversible response of the phototransistor. Figure 3b shows the plot of a photocurrent on/off switching cycle in Figure 3a. It is observed that the photodetector exhibits rapid photocurrent switching. Both the rise and decay times are found to be 7.8 ms, which is comparable to the rise and decay times of state-of-the-art 2D photodetectors. Similarly, a relatively steady photoswitching behavior is also observed for excitations by the 1064 nm and 1340 nm laser under the same test condition, as displayed in Figure 3c. These phenomena further confirm that the outstanding photoresponse in the near-infrared region stems from as-synthesized PbS nanoplates. Moreover, it is worth noting that the photocurrent on-off switching ratio is as high as 10^2 at V_{gs} = -20 V and P = 124 mW/cm^2, which indicates an ultrasensitive ability in the detection of infrared light. Indeed, the lateral dimension of as-synthetized PbS nanoplates ranges from 150 to 750 nm, which gives rise to the relatively low surface coverage of PbS nanoplates on the MoS_2. However, a fast response time and high

photoresponsivity could still be realized in our devices for different surface coverage. As shown in Figure S6 a, the rise and decay times of PbS-MoS_2 heterostructures with a coverage of 9% approach 15.6 and 23.4 ms, respectively. Similarly, an ultrafast response time of 7.8 ms is also obtained for the same device with coverage of 37% and 43%, as observed in Figure S6 (b-c). This indicates that the response time is less affected by the coverage area of PbS. Moreover, we plotted the responsivity as a function of surface coverage of PbS. Figure S6 d shows that the responsivity exhibits an increased trend as the coverage of PbS increases. We attribute the fast and sensitive response to the novel edge-contact between MoS_2 and PbS nanoplates. There are three key factors that determine the high performance of the phototransistor. Firstly, PbS nanoplates contact with MoS_2 edges by a strong chemical hybridization, which is expected to offer a fast transmission path for carriers that enhances the response speed. Secondly, PbS nanoplates are highly single-crystalline (Fig. 1d), and they provide a long-range order for the electronic transport path with reduced boundary defect states where scattering can occur. Finally, the vdW interaction distance in our heterostructures should be smaller than that in hybrid colloidal PbS quantum dot-MoS_2 structures,[15, 38] which is beneficial for the transfer of photogenerated electrons from PbS to MoS_2. Significantly, the edge-contact plays a crucial role in the high performance of the phototransistor because the seamless contact between PbS and MoS_2 through the chemical bonding interaction aids carrier transport in the interface. Recently, a low average contact resistance of 30 kΩ.μm has been achieved for the graphene and TMD layer with edge contacts.[39] Although the area of the edge-contact is much smaller than that of the total interface, it can provide a lower contact resistance and enhance the transfer of photogenerated electrons from PbS to MoS_2. A detailed explanation and theoretical simulation will be discussed below.

From our experiments, we clearly observe an interesting phenomenon of PbS nanoplates-MoS_2 heterostructures where all of the PbS nanoplates are in contact with the edges of MoS_2 along the <110> direction. Simultaneously, the abundant unsaturated Mo atoms on the edge of MoS_2 result in a high activity of the edge area. This fact indicates the possibility that the PbS nanoplates is primarily nucleated at the edge, and the heterostructures were mainly maintained by the chemical bonds on the edge-contact area. Hence, to verify the viewpoints proposed above, we calculated the binding energy of the edge-contact model. The binding energy is defined as follows：

$$E_{bind}=(E_{PbS/MoS2}-E_{PbS}-E_{MoS2}) /N \quad (1\text{-}1)$$

where $E_{PbS/MoS2}$ represents the total energy of the PbS-MoS_2 heterostructures, and E_{PbS} and E_{MoS2} represent the total energy of the PbS and MoS_2, respectively; moreover, N represents the number of Mo-S bonds that are formed between Mo of MoS_2 and S of PbS (110). To verify the chemical bonding on the edge, we calculated the charge density difference ρ, which is defined as follows:

$$\rho=\rho(PbS/MoS_2)-\rho(PbS)-\rho(MoS_2) \quad (1\text{-}2)$$

where $\rho(PbS/MoS_2)$, $\rho(PbS)$, $\rho(MoS_2)$ represents the charge density of the PbS/MoS_2 edge-contact model, PbS(110) and MoS_2 nanoribbon, respectively.

The schematic diagram of the edge-contact between the MoS_2 and PbS is presented in Figure 4a. The Mo atoms of the zigzag edge of MoS_2 were bonded with the S atom chain that is exposed to PbS (110). The inset is a top view of the schematic diagram. In our calculations, due to the very low lattice mismatch (0.1%) along the zigzag direction of MoS_2, each Mo atom perfectly bonded with two S atoms. Therefore, there are 6 Mo-S bonds in the edge-contact region in a repeat unit. Additionally, every single bond length was marked in Figure. 4b. We clearly obtained an average Mo-S bond ca. 2.433 Å in the edge-contact region, which is similar with the value in MoS_2 (2.412 Å). Furthermore, the binding energy of the edge-contact model is -1.73eV per Mo-S bond. Both the bond length and binding energy indicated that the chemical bonds were formed in the edge-contact region. For further confirmation, we calculated the charge density difference (Figure. 4c) and PDOS (Figure. 4d) of the edge-contact region. Here, the red region indicates the charge accumulation region and the green region indicates the charge depletion region in Figure. 4c. We clearly observe that the charge density increases in the bonding region and decreases around the Mo-S bonds; in addition, the charge density increases to a larger extent at the Mo atoms. In other words, it is obvious that the ionic bonds were formed in the edge-contact region. Moreover, the bonding detail was presented by the PDOS of the edge-contact region, as observed in Figure. 4d. The Mo-4d orbital and S-3p orbital clearly undergo orbital hybridization. Overall, the evidence from both the binding energy and electronic structure indicate that an ionic bond is formed by the S-3p and Mo-4d in the edge-contact region.

Periodic arrays have shown superiority in active matrix displays and sensor arrays, which require minimal cross-talk between neighboring devices. In addition, detector technologies should be compatible with

traditional metal-oxide semiconductor (CMOS) electronics for integration into high-sensitivity sensing and imaging systems. Therefore, integrated PbS-MoS_2 heterostructure periodic arrays on Si chips are of great importance in practical applications. Figure 5a shows MoS_2 patterning performed by a photolithography process followed by O_2 plasma etching .The width of the MoS_2 pattern is 5 μm. The PbS nanoplates selectively grew on MoS_2 via a carefully controlled growth condition, as displayed in Figure 5b. This behavior could be explained by classical nucleation kinetics. Compared with the larger surface energy of SiO_2 ($\gamma_{SiO2}\approx$ 300–400 mJ m^{-2}), the surface energy of MoS_2 is 70–75 mJm^{-2}.[40, 41] Therefore, epitaxial PbS on SiO_2/Si must overcome a larger free energy barrier. In contrast, the growth of PbS on MoS_2 should be relatively easy. In particular, PbS nanoplates grew on the entire MoS_2 pattern. This phenomenon could be attributed to the presence of photoresist residues as a result of the photolithography process because PbS is easily nucleated at certain defect sites. As is evident from Figure 5c, PbS nanoplates-MoS_2 heterostructures 3×3 arrays were directly fabricated by electron beam lithography for practical high-performance infrared phototransistor applications; this indicates the potential scalability of our heterostructure. Figure 5d shows a schematic illustration of the PbS nanoplates-MoS_2 heterostructure arrays. As observed in Figure S5 c, although the device from the PbS-MoS_2 pattern exhibits rapid photoswitching speeds of τ_{rising} = 51.3 ms and τ_{decay}=102.7 ms, the photoswitching speeds are much slower than those of the previously mentioned edge-contact heterostructure. The photoresist residues can act as trap state centers, which can trap the photo-excited carriers. The performance will be improved and the potential trapping will be overcome as the fabrication technology becomes mature.

In summary, we have synthesized non-layered PbS and layered MoS_2 heterostructures via van der Waals epitaxy. The device exhibits fast response (τ_{rising}= τ_{decay}=7.8 ms), high photoresponsivity (4.5×10^4 AW^{-1}) and I_{light}/I_{dark} (1.3×10^2), and an ultrahigh detectivity of 3×10^{13} Jones. In addition, the photoresponse wavelengths extend to the infrared region (0.8-1.34 um). Moreover, in conjunction with density functional theory (DFT) calculations, we elucidate that PbS nanoplates form edge-contacts with MoS_2 via a strong chemical hybridization. Furthermore, we achieved precise control of the PbS nanoplates-MoS_2 heterostructure periodic arrays on the Si/SiO_2 substrate. This study enables the large-scale fabrication of PbS-MoS_2 phototransistors for practical high-performance photodetector applications.

Methods

Device fabrication. Large-area MoS_2 was synthesized by chemical vapor deposition (CVD) from molybdenum trioxide (MoO_3) and pure sulfur powders. Insulating SiO_2/Si layers were used as the growth substrates, and the zone with MoO_3 is heated to 850 ℃. The process is performed at atmospheric pressure under the flow of ultrahigh-purity argon. The mechanically exfoliated MoS_2 was prepared by standard mechanical exfoliation with scotch tape. The PbS powder was thermally evaporated into vapor molecules and then self-assembled into single crystalline nanoplates on MoS_2 under a flow of 20 sccm of H_2 gas. The source and substrate temperatures were set to 750 °C and 500 °C, respectively. Back-gated phototransistors were fabricated on n-doped silicon substrates. Electron beam lithography (EBL) was employed to pattern source/drain electrodes on as-synthesized PbS-MoS_2 heterostructures. Subsequently, metal electrodes (Cr/Au, 10 nm/ 60 nm) were deposited by thermal evaporation.

Microstructure characterization. The PbS nanoplates-MoS_2 heterostructure was characterized by optical microscopy (Leica DM4000M microscope), FESEM S4800 (Tokyo, Japan), AFM (Dimension 3100), FEI Tecnai F20 equipped with SAED, and Raman spectroscopy (Renishaw InVia, 532 nm excitation laser).

DFT computational details. The structural properties of MoS_2 and PbS were calculated by density functional theory (DFT), which was performed by the Vienna Ab Initio Simulation Package (VASP) version 5.3.5. [42, 43] The projector augmented wave potentials and GGA functional of PBE were applied. [44, 45] A kinetic energy cutoff of 500 eV was set for wave functions in a plane-wave basis. For representing the experiment, we simulated the edge-contact between MoS_2 and PbS by adopting the MoS_2 ribbons model and the PbS (110), whose surface is composed of Pb atomic chains and S atomic chains. Hence, 1×9×1 Monkhorst–Pack k-point meshes[46] for the edge-contact model and a vacuum region of ~15 Å along the Z-direction were used to achieve the converged results. In addition, all the MoS_2 and only two layers of the PbS slab were relaxed until the maximum Hellmann–Feynman force acting on each atom was less than 0.03 eV/Å and the convergence for the total energy between two consecutive steps was less than 1×10^{-4} eV.

Photoresponse measurement. All the measurements were performed by a manual probe station at room temperature. The devices were placed in a sealed chamber at a vacuum of 10^{-6} torr. The parameters were analyzed using a Keithley 4200 semiconductor characterization system.

ASSOCIATED CONTENT

Supporting Information

Experimental details, AFM images, SAED, Raman spectra. This material is available free of charge via the Internet at http://pubs.acs.org.

AUTHOR INFORMATION

Corresponding Author

*Email: hej@nanoctr.cn

Notes

The authors declare no competing financial interest. †These authors contributed equally to the work.

ACKNOWLEDGMENTS

This work was supported by the National Natural Science Foundation of China (Nos. 21373065, 61474033 and 61574050), the Strategic Priority Research Program of the Chinese Academy of Sciences (Grant No. XDA09040201), the 973 Program of the Ministry of Science and Technology of China (No. 2012CB934103), and the CAS Key Laboratory of Nanosystem and Hierarchical Fabrication. The authors gratefully acknowledge the support of the Youth Innovation Promotion Association, CAS.

Rereferences

1. Cui, X.; Lee, G.-H.; Kim, Y. D.; Arefe, G.; Huang, P. Y.; Lee, C.-H.; Chenet, D. A.; Zhang, X.; Wang, L.; Ye, F.; Pizzocchero, F.; Jessen, B. S.; Watanabe, K.; Taniguchi, T.; Muller, D. A.; Low, T.; Kim, P.; Hone, J. *Nat. Nano.* **2015,** 10, (6), 534-540.

2. Wang, Q. H.; Kalantar-Zadeh, K.; Kis, A.; Coleman, J. N.; Strano, M. S. *Nat. Nano.* **2012,** 7, (11), 699-712.

3. Liu, Y.; Weiss, N. O.; Duan, X.; Cheng, H.-C.; Huang, Y.; Duan, X. *Nat. Rev. Mater.* **2016**, 16042.

4. Tian, H.; Chin, M. L.; Najmaei, S.; Guo, Q.; Xia, F.; Wang, H.; Dubey, M. *Nano Res.* **2016,** 9, (6), 1543-1560.

5. Li, Z.; Chang, S.-W.; Chen, C.-C.; Cronin, S. B. *Nano Res.* **2014,** 7, (7), 973-980.

6. Cho, E. H.; Song, W. G.; Park, C. J.; Kim, J.; Kim, S.; Joo, J. *Nano Res.* **2015,** 8, (3), 790-800.

7. Cheng, R.; Li, D.; Zhou, H.; Wang, C.; Yin, A.; Jiang, S.; Liu, Y.; Chen, Y.; Huang, Y.; Duan, X. *Nano Lett.* **2014,** 14, (10), 5590-5597.

8. Huang, X.; Zeng, Z.; Zhang, H. *Chem. Soc. Rev.* **2013,** 42, (5), 1934-1946.

9. Duan, X.; Wang, C.; Pan, A.; Yu, R.; Duan, X. *Chem. Soc. Rev.* **2015,** 44, (24), 8859-8876.

10. Yin, Z.; Zhang, X.; Cai, Y.; Chen, J.; Wong, J. I.; Tay, Y.-Y.; Chai, J.; Wu, J.; Zeng, Z.; Zheng, B.; Yang, H. Y.; Zhang, H. *Angew. Chem. Int. Ed.* **2014,** 53, (46), 12560-12565.

11. Zhang, H. *ACS Nano.* **2015,** 9, (10), 9451-9469.

12. Kuc, A.; Zibouche, N.; Heine, T. *Phys. Rev. B.* **2011,** 83, (24), 245213.

13. RadisavljevicB; RadenovicA; BrivioJ; GiacomettiV; KisA. *Nat. Nano.* **2011,** 6, (3), 147-150.

14. Li, H.; Wu, J.; Yin, Z.; Zhang, H. *Acc. Chem. Res.* **2014,** 47, (4), 1067-1075.

15. Kufer, D.; Nikitskiy, I.; Lasanta, T.; Navickaite, G.; Koppens, F. H. L.; Konstantatos, G. *Adv. Mater.* **2015,** 27, (1), 176-180.

16. Konstantatos, G.; Howard, I.; Fischer, A.; Hoogland, S.; Clifford, J.; Klem, E.; Levina, L.; Sargent, E. H. *Nature.* **2006,** 442, (7099), 180-183.

17. McDonald, S. A.; Konstantatos, G.; Zhang, S.; Cyr, P. W.; Klem, E. J. D.; Levina, L.; Sargent, E. H. *Nat. Mater.* **2005,** 4, (2), 138-142.

18. Konstantatos, G.; Badioli, M.; Gaudreau, L.; Osmond, J.; Bernechea, M.; de Arquer, F. P. G.; Gatti, F.; Koppens, F. H. L. *Nat. Nano.* **2012,** 7, (6), 363-368.

19. Allain, A.; Kang, J.; Banerjee, K.; Kis, A. *Nat. Mater.* **2015,** 14, (12), 1195-1205.

20. Wang, X.; Wang, P.; Wang, J.; Hu, W.; Zhou, X.; Guo, N.; Huang, H.; Sun, S.; Shen, H.; Lin, T.; Tang, M.; Liao, L.; Jiang, A.; Sun, J.; Meng, X.; Chen, X.; Lu, W.; Chu, J. *Adv. Mater.* **2015,** 27, (42), 6575-6581.

21. Lopez-Sanchez, O.; Lembke, D.; Kayci, M.; Radenovic, A.; Kis, A. *Nat. Nano.* **2013,** 8, (7), 497-501.

22. Nikitskiy, I.; Goossens, S.; Kufer, D.; Lasanta, T.; Navickaite, G.; Koppens, F. H. L.; Konstantatos, G. *Nat. Commun.* **2016,** 7, 11954.

23. Briseno, A. L.; Mannsfeld, S. C. B.; Ling, M. M.; Liu, S.; Tseng, R. J.; Reese, C.; Roberts, M. E.; Yang, Y.; Wudl, F.; Bao, Z. *Nature.* **2006,** 444, (7121), 913-917.

24. Han, G. H.; Kybert, N. J.; Naylor, C. H.; Lee, B. S.; Ping, J.; Park, J. H.; Kang, J.; Lee, S. Y.; Lee, Y. H.; Agarwal, R.; Johnson, A. T. C. *Nat. Commun.* **2015,** 6, 6128.

25. Liao, L.; Bai, J.; Cheng, R.; Zhou, H.; Liu, L.; Liu, Y.; Huang, Y.; Duan, X. *Nano Lett.* **2012,** 12, (6), 2653-2657.

26. Oh, S.; Park, S. K.; Kim, J. H.; Cho, I.; Kim, H.-J.; Park, S. Y. *ACS Nano.* **2016**.

27. Yu, Q.; Jauregui, L. A.; Wu, W.; Colby, R.; Tian, J.; Su, Z.; Cao, H.; Liu, Z.; Pandey, D.; Wei, D.; Chung, T. F.; Peng, P.; Guisinger, N. P.; Stach, E. A.; Bao, J.; Pei, S.-S.; Chen, Y. P. *Nat. Mater.* **2011,** 10, (6), 443-449.

28. Gan, X.; Shiue, R.-J.; Gao, Y.; Meric, I.; Heinz, T. F.; Shepard, K.; Hone, J.; Assefa, S.; Englund, D. *Nat. Photon.* **2013,** 7, (11), 883-887.

29. Wen, Y.; Wang, Q.; Yin, L.; Liu, Q.; Wang, F.; Wang, F.; Wang, Z.; Liu, K.; Xu, K.; Huang, Y.; Shifa, T. A.; Jiang, C.; Xiong, J.; He, J. *Adv. Mater.* **2016**, 28, (36), 8051-8057.

30. Schmidt, H.; Wang, S. F.; Chu, L. Q.; Toh, M.; Kumar, R.; Zhao, W. J.; Neto, A. H. C.; Martin, J.; Adam, S.; Ozyilmaz, B.; Eda, G. *Nano Lett.* **2014,** 14, (4), 1909-1913.

31. Yao, W.; Xunzhong, S.; Ji, D.; Kai, X.; Jun, H.; Chao, J. *Nanotechnology.* **2015,** 26, (27), 275601.

32. Wang, Q.; Safdar, M.; Xu, K.; Mirza, M.; Wang, Z.; He, J. *ACS Nano.* **2014,** 8, (7), 7497-7505.

33. Wang, Q.; Xu, K.; Wang, Z.; Wang, F.; Huang, Y.; Safdar, M.; Zhan, X.; Wang, F.; Cheng, Z.; He, J. *Nano Lett.* **2015,** 15, (2), 1183-1189.

34. Wang, Q.; Wen, Y.; Yao, F.; Huang, Y.; Wang, Z.; Li, M.; Zhan, X.; Xu, K.; Wang, F.; Wang, F.; Li, J.; Liu, K.; Jiang, C.; Liu, F.; He, J. *Small.* **2015,** 11, (40), 5388-5394.

35. Niu, L.; Liu, X.; Cong, C.; Wu, C.; Wu, D.; Chang, T. R.; Wang, H.; Zeng, Q.; Zhou, J.; Wang, X.; Fu, W.; Yu, P.; Fu, Q.; Najmaei, S.; Zhang, Z.; Yakobson, B. I.; Tay, B. K.; Zhou, W.; Jeng, H. T.; Lin, H.; Sum, T. C.; Jin, C.; He, H.; Yu, T.; Liu, Z. *Adv. Mater.* **2015,** 27, (47), 7800-7808.

36. Nichols, P. L.; Liu, Z.; Yin, L.; Turkdogan, S.; Fan, F.; Ning, C. Z. *Nano Lett.* **2015,** 15, (2), 909-916.

37. Wang, F.; Wang, Z.; Xu, K.; Wang, F.; Wang, Q.; Huang, Y.; Yin, L.; He, J. *Nano Lett.* **2015,** 15, (11), 7558–7566.

38. Wang, Q.; Wen, Y.; He, P.; Yin, L.; Wang, Z.; Wang, F.; Xu, K.; Huang, Y.; Wang, F.; Jiang, C.; He, J. *Adv. Mater.* **2016,** 28, (30), 6497-6503.

39. Guimarães, M. H. D.; Gao, H.; Han, Y.; Kang, K.; Xie, S.; Kim, C.-J.; Muller, D. A.; Ralph, D. C.; Park, J. *ACS Nano.* **2016,** 10, (6), 6392-6399.

40. Zheng, W.; Feng, W.; Zhang, X.; Chen, X.; Liu, G.; Qiu, Y.; Hasan, T.; Tan, P.; Hu, P. A. *Adv. Funct. Mater.* **2016,** 26, (16), 2648-2654.

41. Heo, H.; Sung, J. H.; Jin, G.; Ahn, J.-H.; Kim, K.; Lee, M.-J.; Cha, S.; Choi, H.; Jo, M.-H. *Adv. Mater.* **2015,** 27, (25), 3803-3810.

42. Kresse, G.; Furthmüller, J. *Phys. Rev. B.* **1996,** 54, (16), 11169-11186.

43. Kresse, G.; Furthmüller, J. *Comput. Mater. Sci.* **1996,** 6, (1), 15-50.

44. Blöchl, P. E. *Phys. Rev. B.* **1994,** 50, (24), 17953-17979.

45. Perdew, J. P.; Burke, K.; Ernzerhof, M. *Phys. Rev. Lett.* **1996,** 77, (18), 3865-3868.

46. Monkhorst, H. J.; Pack, J. D. *Phys. Rev. B.* **1976,** 13, (12), 5188-5192.

47. Gong, X.; Tong, M.; Xia, Y.; Cai, W.; Moon, J. S.; Cao, Y.; Yu, G.; Shieh, C.-L.; Nilsson, B.; Heeger, A. J. *Science.* **2009,** 325, (5948), 1665-1667.

48. Zheng, D.; Wang, J.; Hu, W.; Liao, L.; Fang, H.; Guo, N.; Wang, P.; Gong, F.; Wang, X.; Fan, Z.; Wu, X.; Meng, X.; Chen, X.; Lu, W. *Nano Lett.* **2016,** 16, (4), 2548-2555.

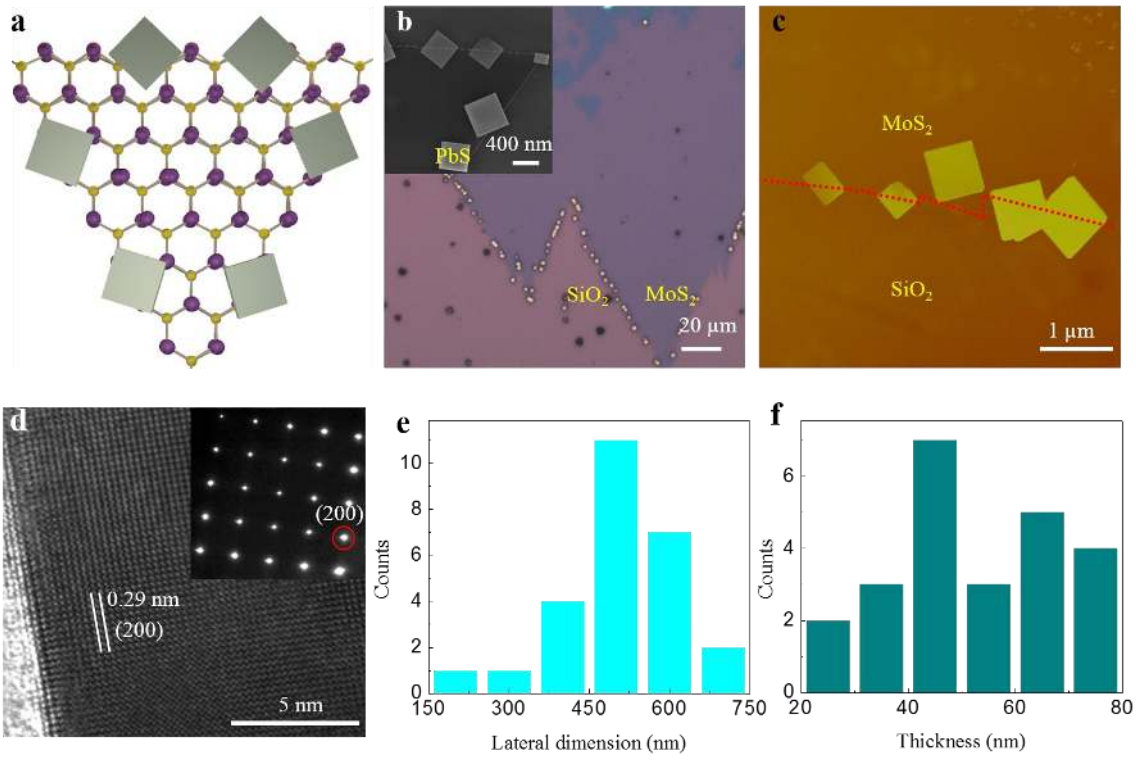

Figure 1. Morphology of non-layered PbS nanoplates-MoS_2 heterostructures. (a) Schematic illustration of PbS nanoplates-MoS_2 heterostructures. (b) OM image with selectively growing PbS nanoplates along the edge of MoS_2 triangle. The inset in (b) is an amplified SEM image of edge contact heterostructures. (c) AFM image of edge of MoS_2 triangle. (d) HRTEM image with crystal fringes of (200) planes. The SAED cubic pattern is shown in the inset of (d). The histogram statistics of PbS nanoplates: the lateral dimension and thickness distribution ranging from 150 to 750 nm and 20 to 80 nm, respectively.

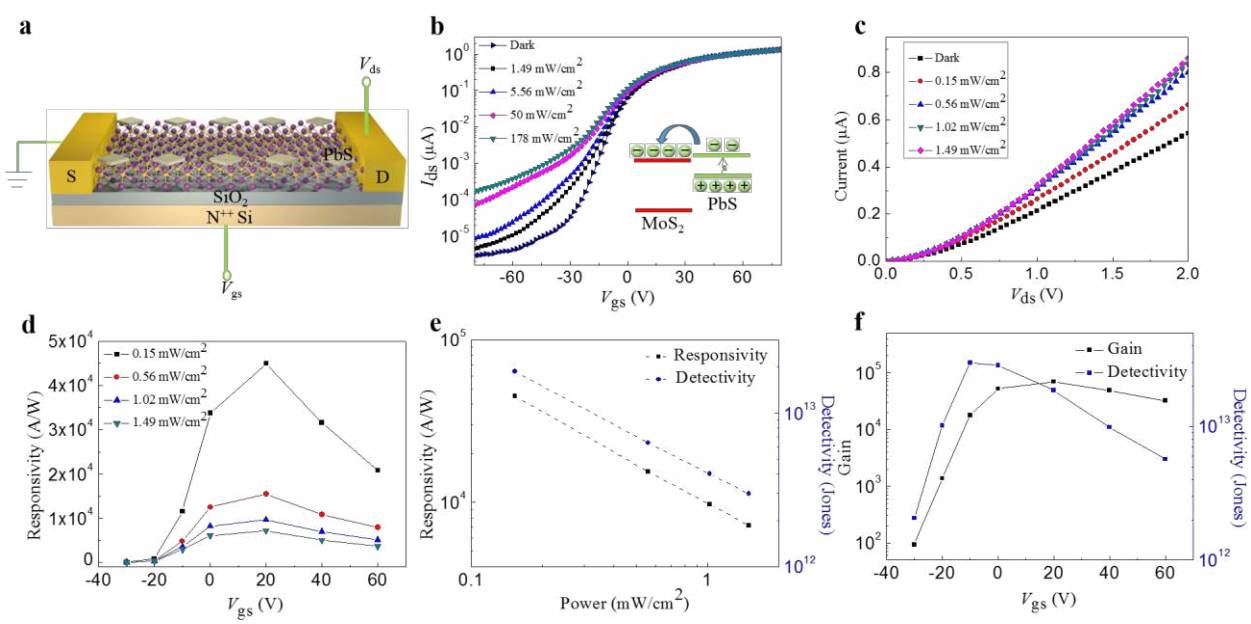

Figure 2. Gate voltage-tunable responsivity and detectivity of epitaxial PbS nanoplates-MoS_2 heterostructures. (a) Schematic of a typical device. (b) Transfer characteristic (I_{ds}-V_{gs}) measurements under laser illumination (wavelength, λ = 800 nm) with power densities varied from 1.49 to 178 mW/cm^2 were performed at V_{ds} = 2 V and T = 300 K. (c) The output characteristic (I_{ds}-V_{ds}) curves with different power densities at V_{gs} = 20 V. (d) The responsivity of the heterostructures is plotted as a function of the applied back-gated voltage. (e) The plots of R and D^* versus P for different power densities at V_{gs} = 20 V. (f) The gate-tunable behavior for photo-gain (G) and detectivity with P = 0.15 mW/cm^2.

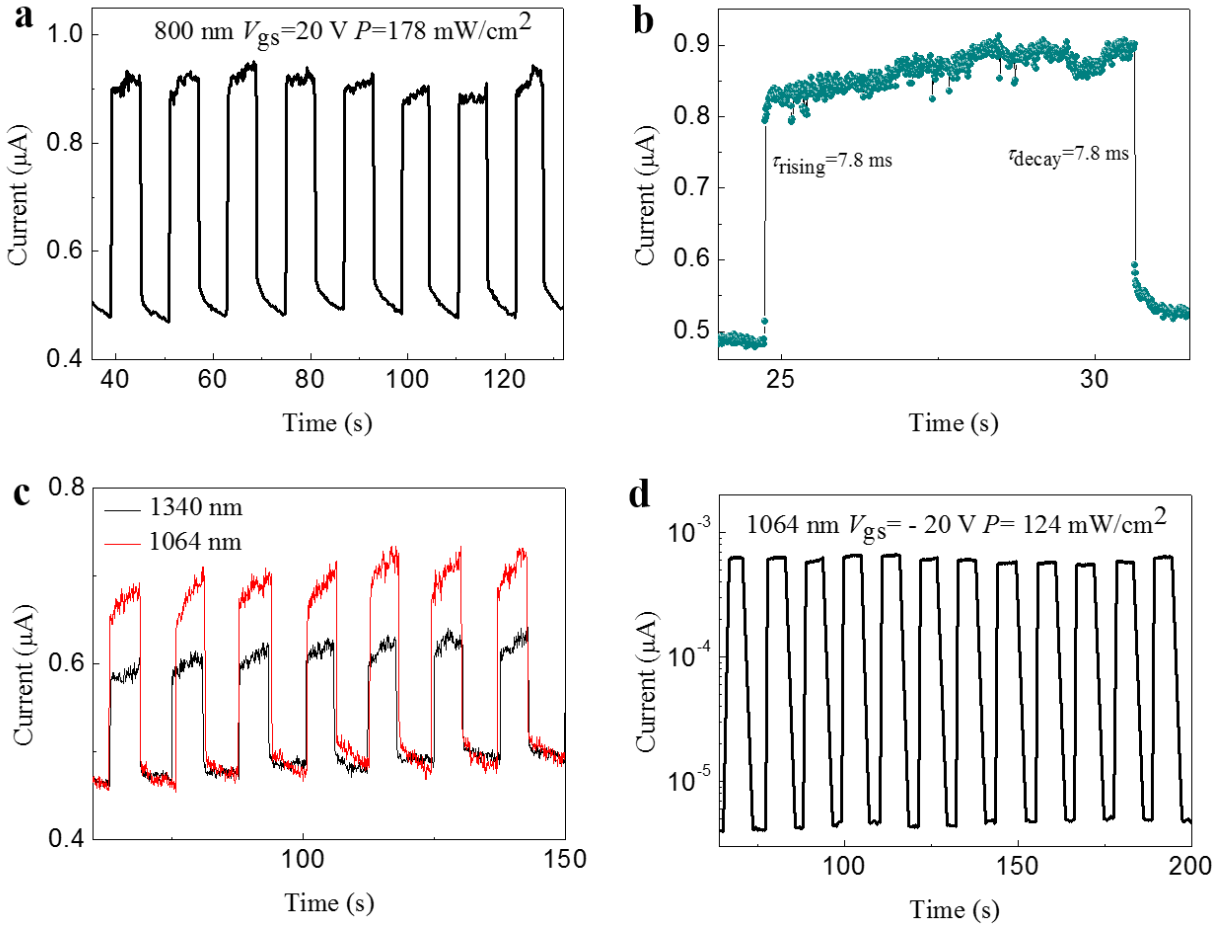

Figure 3. Time-resolved photoresponse of epitaxial PbS nanoplates-MoS_2 heterostructures. (a) Time-resolved photoresponse was measured at 800 nm, which indicates a highly stable and reversible response of the phototransistor. (b) Temporal response exhibits fast photoswitching (τ_{rising}= τ_{decay}= 7.8 ms). (c) Time-resolved photoresponse in the near-infrared region at 1064, 1340 nm with power densities of 124 and 145 mW/cm^2, respectively. (d) The ratio of photocurrent on-off switching is as high as 10^2 at V_{gs} = -20 V and P = 124 mW/cm^2.

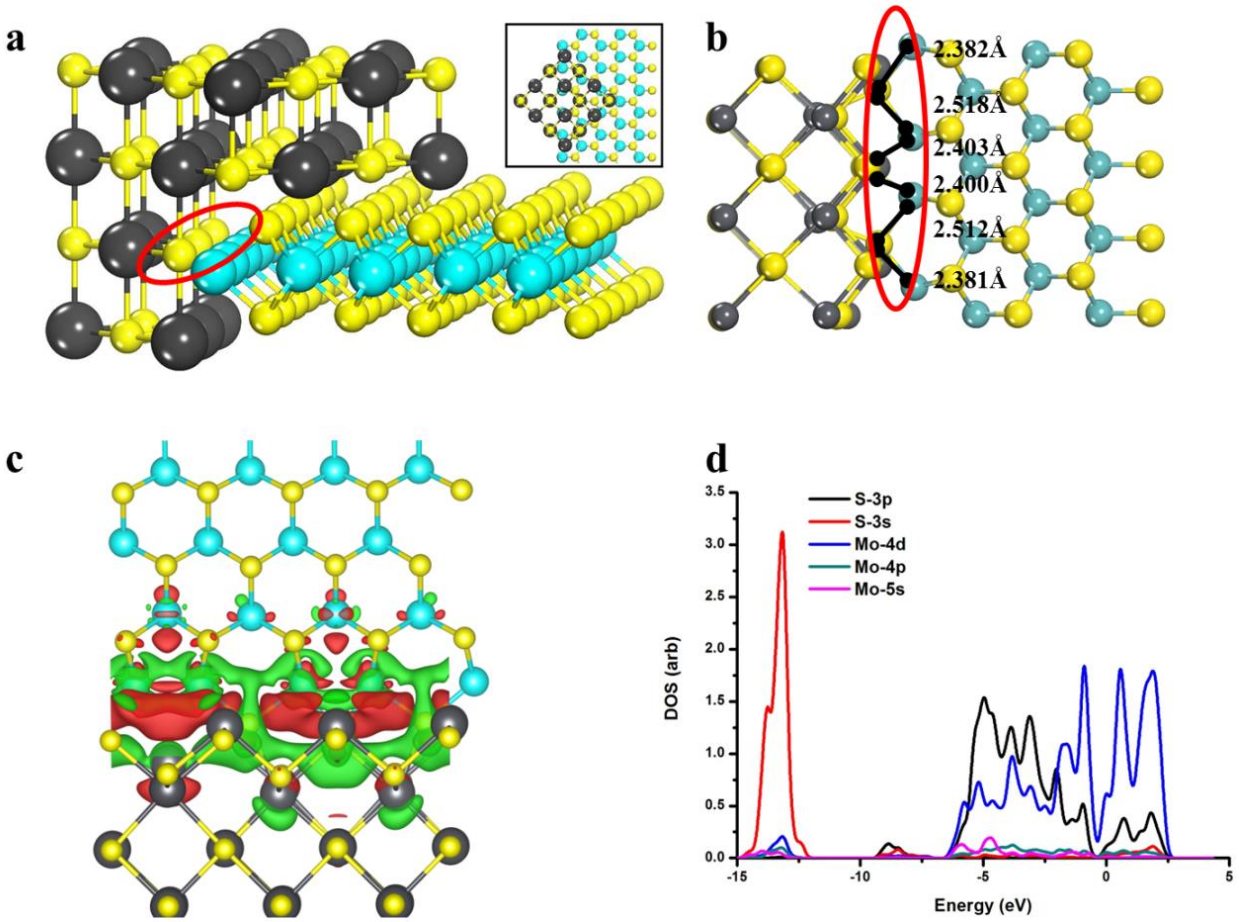

Figure 4. The edge-contacts of PbS nanoplates-MoS_2 heterostructures were calculated by density functional theory (DFT) (a) The schematic diagram of edge-contact between the MoS_2 and PbS, and the inset is a top view of the schematic diagram. (b) The bonding situation in the edge-contact region. (c) The charge density difference of the edge-contact; the red and green regions represent charge accumulation and depletion regions, respectively. (d) PDOS of the edge-contact region, the Fermi energy was set to zero. The black ball is C, the yellow ball is S and the blue-green ball is Mo.

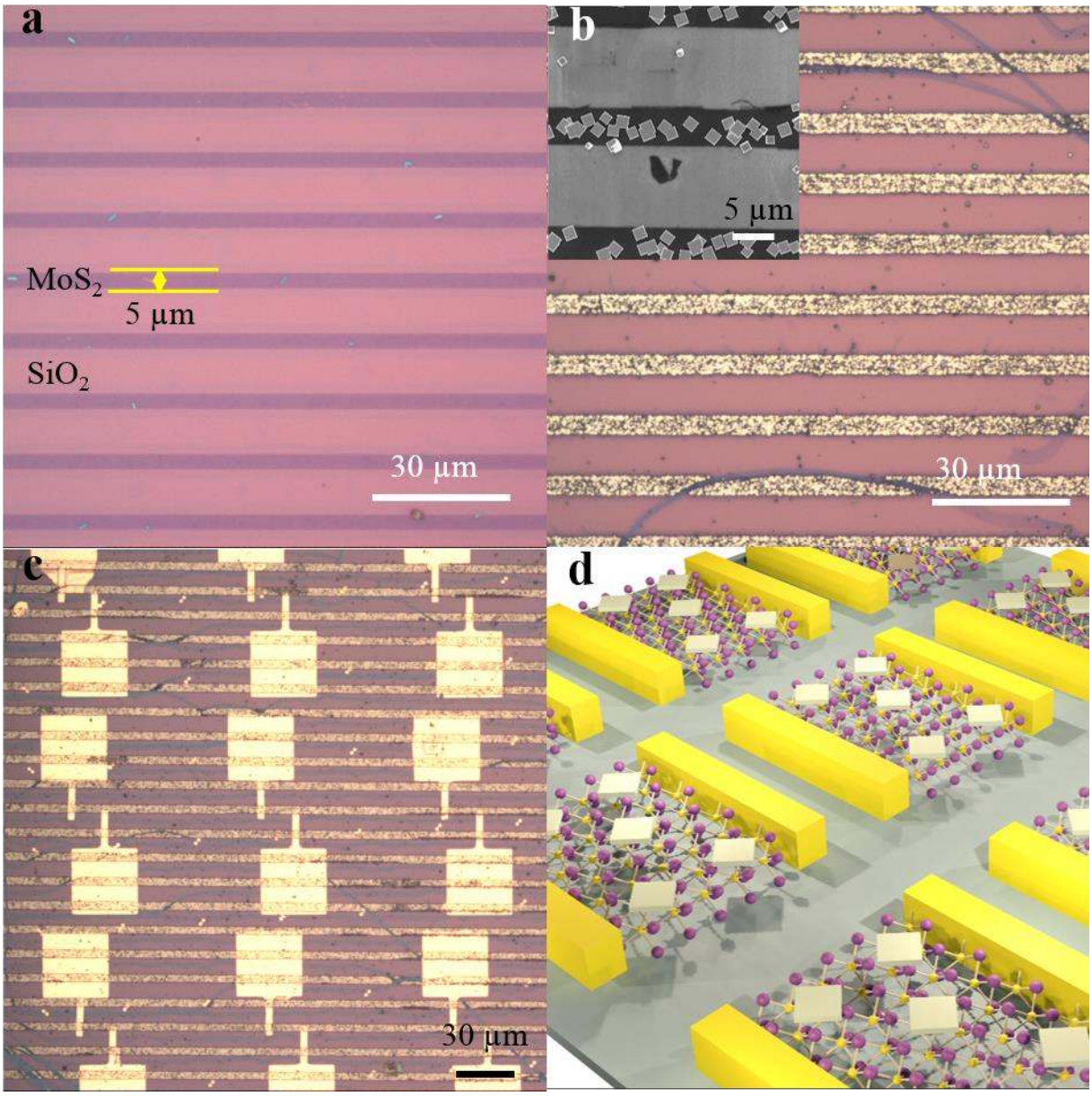

Figure 5. Scalable fabrication of the heterostructure. (a) MoS_2 patterning by a photolithography process followed by O_2 plasma etching. (b) The PbS nanoplates selectively grew on MoS_2 via a carefully controlled growth condition. (c) The PbS nanoplates-MoS_2 heterostructure 3×3 arrays were directly fabricated by an electron beam lithography process. (d) Schematic illustration of PbS nanoplates-MoS_2 heterostructure arrays.

	Wavelength	Response time	I_{ph}/I_{dark}	Detectivity	Responsivity	Ref.
commercial Si	-	-	-	$\sim 10^{12}$	-	47
commercial InGaAs	-	-	-	$\sim 10^{12}$	-	48
GaAs/AlGaAs NW	-	-	10^2	7.2×10^{10}	0.57 AW^{-1}	47
CdS-MoS_2	610 nm	τ_{rising}= 100 ms	-	-	3.91 AW^{-1}	40
PbS quantum dots-MoS_2	635 nm	τ_{decay}= 350 ms	-	$\sim 10^{11}$ ($V_g = -60$ V)	6×10^5 AW^{-1}	15
PbS nanoplates-MoS_2	800 nm	τ_{rising}= τ_{decay}= 7.8 ms	10^2	10^{13} (V_g = 0 V)	4.5×10^4 AW^{-1}	This work

Table 1. Comparison of critical optoelectronic parameters in various photodetectors.